IEEE Access
Multidisciplinary ⋮ Rapid Review ⋮ Open Access Journal

Received September 13, 2020, accepted September 15, 2020, date of publication September 28, 2020,
date of current version October 9, 2020.

Digital Object Identifier 10.1109/ACCESS.2020.3027310

Compensation Module Design for Overlapping Band in Band-Interleaved Data Acquisition Systems Based on Hybrid Particle Swarm Optimization Algorithm

YU ZHAO[1], PENG YE[1,2], JIE MENG[1], (Graduate Student Member, IEEE), KUOJUN YANG[1], (Member, IEEE), JIAN GAO[1], (Member, IEEE), ZHIXIANG PAN[1], WUHUANG HUANG[1], (Member, IEEE), JINPENG SONG[3], (Member, IEEE), AND XUEFENG DAI[1]

[1]School of Automation Engineering, University of Electronic Science and Technology of China, Chengdu 611731, China
[2]Department of Research and Development, Uni-Trend Technology (China), Dongguan 523000, China
[3]School of Information and Electronics, Beijing Institute of Technology, Beijing 100081, China

Corresponding authors: Kuojun Yang (yangkuojun@uestc.edu.cn) and Peng Ye (yepeng_uestec@163.com)

This work was supported in part by the National Natural Science Foundation of China under Grant 61901037, Grant 61801092, and Grant 61701077, in part by the Fundamental Research Fund for the Central University of China under Grant ZYGX2019J065, and in part by the Dongguan Introduction Program of Leading Innovative and Entrepreneurial Talents.

ABSTRACT The band interleaved data acquisition system (BI-DAS) is an attractive structure to improve the bandwidth of the acquisition system. However, the non-ideal characteristic of the spectrum analysis filter in BI-DAS results in an overlapping frequency band between two adjacent frequency sub-bands. Phase misalignment (PM) between two sub-bands in the overlapping band may cause those signals canceled or partially canceled to each other when sub-bands' signal are merged. In this paper, a compensation module with a digital all-pass filter (APF) is proposed for the PM of the overlapping bands in BI-DASs. Based on this compensation module, a hybrid Particle Swarm Optimization (PSO) algorithm, along with the Levenberg-Marquardt (LM) algorithm is proposed to design coefficients of the compensation module. The compensation module and corresponding method proposed in this paper are verified in a BI-DAS with 20Gsps sampling rate and 5.5GHz bandwidth. The experimental results show that the proposed compensation module can effectively compensate the PM between the sub-bands in the overlapping band. The proposed hybrid PSO-LM (HPSOLM) algorithm combines the flexibility and reliability inherent in the PSO with the fast convergence and precision of the LM algorithm. It can effectively design the compensation module with stable APF while consuming less time and obtaining better compensation results than the conventional PSO method.

INDEX TERMS Band interleaved data acquisition system, overlapping band, phase compensation, digital all-pass filters, hybrid particle swarm optimization algorithm, Levenberg-Marquardt algorithm.

I. INTRODUCTION

To keep abreast of the exploding frequency of signals in electronic systems, the bandwidth of the data acquisition system (DAS) in the electronic equipment, such as communication receivers and electronic instruments, is up to tens or even hundreds of GHz [1]–[3]. As the core device of the acquisition system, analog-to-digital converter (ADC) significantly defines the upper limit of the DAS's bandwidth. In the foreseeable future, the upcoming improvement nodes of complementary metal oxide semiconductor (CMOS) ADC do not adapt the expected bandwidth requirement for the next generation DAS. To resolve this contradiction, parallel DAS architectures, e.g., band-interleaved (BI) DAS [4], [5], frequency-interleaved (FI) DAS [6], [7] and asynchronous time-interleaved (ATI) DAS [8], etc., are attractive solutions

The associate editor coordinating the review of this manuscript and approving it for publication was Abdel-Hamid Soliman.

that transcend the limitation imposed by traditional CMOS ADC devices.

These parallel DAS architectures have a similar strategy, which transfers the high-frequency signals to the baseband, and recovers the signals at the digital back-end after sampling with a low bandwidth ADC. Taking BI-DAS as an example, BI-DAS divides the frequency of the broadband signal into several narrow sub-bands by analog filters, and transfer the high-frequency sub-bands to the low-frequency bands by analog down-conversion, to reduce the bandwidth pressure of the ADC. The signals of each sub-band are converted back to their original frequency band by digital signal processing after the ADC quantifies the signals in each sub-band. After that, the signals of multiple frequency bands are merged in the digital domain to recover the original signals.

However, due to the transition region of analog filters, signals in a particular frequency band will appear in two adjacent sub-bands simultaneously, which is called the overlapping band [9]. Phase misalignment (PM) between two sub-bands in the overlapping band may cause those signals canceled or partially canceled to each other when merging the sub-bands' signal. The resulting combined frequency response may accordingly have an undesirable attenuated magnitude response in the overlapping band.

Albert. T [9] proposed a method for the PM in the overlapping band based on the cross-spectrum between two sub-bands. However, this method is under the assumption that the PM between two sub-bands is linear. In practice, the analog filters usually have steep cutoffs to ensure the accuracy of frequency segmentation. These sharp cutoffs introduce the phase nonlinearity in the region around the cutoff frequency as well as the nonlinear PM in the overlapping band, which invalidates linear PM correction methods. Besides, to the best of our knowledge, there is no literature defining the overlapping bands in BI-DAS.

The all-pass filter (APF) has been widely used in non-linear phase equalization [10]–[13], which significantly affects the phase response while the magnitude response is unity throughout the frequency band. The characteristic doesn't introduce any magnitude distortion to the frequency band makes APF an excellent candidate to compensate the non-linear PM in the overlapping band.

Based on the APF, a novel PM compensation module is proposed for the overlapping band in the BI-DAS. The design of the compensation model can be turned to a parameter optimization problem that minimizes the PM in the overlapping band [14]. Non-linear least squares (NLS) approaches were often used for such parameter optimization problems since the non-linear relationship between the coefficients and the phase response of the APF [10]. However, conventional gradient-based iterative optimization method such as the Levenberg-Marquardt (LM) method is sensitive to the selection of initial value, which may cause the optimization to trap into the local optima [15]. In addition, such algorithms are subordinate to unconstrained optimization algorithms, which may lead to the instability of APF in the compensation model when APF's poles move outside the unit circle during the optimization process.

Recently, meta-heuristic algorithms have received more attention in the solving such NLS optimization problems, such as Genetic Algorithm (GA) [16], [17], Difference Evolution (DE) [18], [19], Ant Colony Optimization (ACO) [20], Artificial Bee Colony (ABC) [21] and Particle Swarm Optimization (PSO) [22], [23] algorithms. These evolutionary algorithms are population-based optimization techniques which incorporate random search and selection strategy for global optimization solution.

Among these algorithms, GA's global search ability is highly dependent on the diversity mechanism, which increases the realization complexity [24]. DE algorithm overcomes the shortcoming of GA's complexity, but it is sensitive to the choice of its control parameters [25]. ACO algorithm has a robust local optimization ability, but for multi-modal problems, it tends to the local optima. Also, the ACO algorithm has a slow descending speed [26]. ABC algorithm has emerged recently for solving the multi-modal problems. Still, some hinders have been observed that the ABC, due to adopting the probabilistic mechanism, consumes more iterative trials and execution compared to the PSO algorithm [24].

Compared with the other meta-heuristic algorithms aforementioned, the PSO algorithm is more comfortable to be implemented and requires a few parameters to adjust. Moreover, the sharing mechanism among particles provides better convergence performance [14]. However, the convergence speed of the PSO algorithm decreases when approaching the global optimal solution, and their optimization results have strong randomness. How to improve the convergence speed and numerical stability of the PSO algorithm has become a vital research topic.

This paper proposes a design method of this compensation module with a stable APF based on the hybrid PSO algorithm. The main contributions of this paper are listed as follows:

1) Based on the two sub-bands BI-DAS, this paper analyzes the effect of the PM in the overlapping band during the combination of sub-bands. A mathematical definition of the overlapping band in BI-DAS is proposed, which provides strict theoretical support for the compensation of the overlapping band.

2) According to the characteristics of the PM in the overlapping band, a novel compensation module is proposed. The proposed compensation module compensates linear and non-linear PM by the combination module of integral delay, fractional delay, and an APF, respectively.

3) A hybrid PSO algorithm designing coefficients of the compensation module both in linear compensation module and APF is proposed. The method utilizes the Levenverg-Marquardt (LM) algorithm to accelerate the convergence speed and reduce the randomness of the PSO algorithm. The introduction of the PSO algorithm eliminates the hassle of the selection of the initial values of the LM algorithm.

4) To avoid the instability of the designed APF in the compensation module introduced by the unconstrained optimization algorithm, i.e., the LM algorithm, a parameterizing process is introduced before utilizing the LM algorithm in the HPSOLM algorithm.

The compensation module and HPSOLM algorithm proposed in this paper is verified in a BI-DAS with 20Gsps sampling rate and 5.5GHz bandwidth. Based on the data from the experimental platform, the superiority and validity of the proposed HPSOLM algorithm are further validated by comparing it with the conventional PSO algorithm. In addition, the impact of the PSO algorithm and the LM algorithm on the proposed HPSOLM is discussed.

The remaining of this paper is organized as follows. Section II introduces the principle of the BI-DAS. In Section III, the definition of the overlapping band and error analysis of PM in the overlapping band is given. Section IV describes the proposed compensation module for PM and the corresponding HPSOLM algorithm. The experimental platform and results are provided in Section V and Section VI, respectively, followed by a conclusion in Section VII.

II. PRINCIPLE OF THE BAND INTERLEAVED DATA ACQUISITION SYSTEM

In a two sub-bands BI-DAS, as illustrated in Fig. 1, the input analog signal $x(t)$ is divided into two frequency bands by the analog analysis filters $H_{a1}(j\Omega)$ and $H_{a2}(j\Omega)$, corresponding to the low-pass filter and band-pass filter, respectively. The higher frequency band is down-converted to the baseband by an analog mixer with the analog local oscillator (LO) whose frequency is denoted as Ω_l.

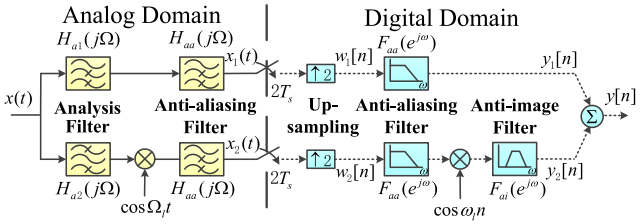

FIGURE 1. Mathematics model of the two channel BI-DAS.

The anti-aliasing filters $H_{aa}(j\Omega)$ are used to avoid the aliasing components of the sampling process. Meanwhile, $H_{aa}(j\Omega)$ in the higher-frequency band also has the function of eliminating the high-frequency image components introduced by the analog down-conversion. Signals before sampling of each sub-band can be illustrated as

$$\begin{cases} X_1(j\Omega) = X(j\Omega)H_{a1}(j\Omega)H_{aa}(j\Omega) \\ X_2(j\Omega) = \dfrac{1}{2}[X(j(\Omega+\Omega_l))H_{a2}(j(\Omega+\Omega_l)) \\ \qquad + X(j(\Omega-\Omega_l))H_{a2}(j(\Omega-\Omega_l))]H_{aa}(j\Omega), \end{cases} \tag{1}$$

where $X(j\Omega), X_1(j\Omega)$ and $X_2(j\Omega)$ are the expressions of $x(t), x_1(t)$ and $x_2(t)$ in the frequency domain, respectively.

In this paper, Ω_l is higher than the high pass-band frequency of $H_{a2}(j\Omega)$, so that the image components of the mixer are away from the baseband and can be eliminated by $H_{aa}(j\Omega)$, a low-pass filter. Note that the effects of frequency interferences and nonlinearity of the analog mixer are irrespective in this paper.

Under the sampling rate of $T_s/2$, where T_s is the sampling rate of the BI-DAS, $x_1(t)$ and $x_2(t)$ are converted into digital signals. The sampling rate is halved to reduce the pressure of the front-end ADC, even though the ADC is still working in over-sampling mode. The sampled signals need to be up-sampled. Otherwise, the following digital up-conversion will introduce the image components into the frequency of interest. Frequency expression of digital signals after up-sampling, $w_m[n]$ $(m = 1, 2)$ can be written as

$$W_m(e^{j\omega}) = \frac{1}{2T_s}\sum_{p=-\infty}^{+\infty} X_m(j\frac{\omega}{T_s} - j\frac{\pi p}{T_s}), \tag{2}$$

where p indexing the frequency replica of sampling and $-\pi \le \omega \le \pi$.

After the up-sampling, the signals in the second sub-band should be up-converted to their original frequency band with digital LO whose frequency is denoted as ω_l, where $\omega_l = \Omega_l T_s$. The final output of each sub-band can be denoted as

$$\begin{cases} Y_1(e^{j\omega}) = W_1(e^{j\omega})F_{aa}(e^{j\omega}) \\ Y_2(e^{j\omega}) = \dfrac{1}{2}[W_2(e^{j(\omega+\omega_l)})F_{aa}(e^{j(\omega+\omega_l)}) \\ \qquad + W_2(e^{j(\omega-\omega_l)})F_{aa}(e^{j(\omega-\omega_l)})]F_{ai}(e^{j\omega}). \end{cases} \tag{3}$$

Since the aliasing errors and image components introduced by up-sampling and digital up-conversion are significantly attenuated by the Anti-aliasing filter $F_{aa}(e^{j\omega})$ and Anti-image filter $F_{ai}(e^{j\omega})$, respectively, only the case of $p = 0$ in (2) is taken into consideration. Substituting the (1) and (2) into (3), (3) can be rewritten as

$$\begin{cases} Y_1(e^{j\omega}) = X(j\dfrac{\omega}{T_s})G_1(e^{j\omega}) \\ Y_2(e^{j\omega}) = X(j\dfrac{\omega}{T_s})G_2(e^{j\omega}), \end{cases} \tag{4}$$

where

$$\begin{aligned} G_1(e^{j\omega}) &= \frac{1}{T_s}H_{a1}(j\frac{\omega}{T_s})H_{aa}(j\frac{\omega}{T_s})F_{aa}(e^{j\omega}) \\ &= M_1(\omega)e^{j\phi_1(\omega)}, \end{aligned} \tag{5}$$

$$\begin{aligned} G_2(e^{j\omega}) &= \frac{1}{T_s}F_{ai}(e^{j\omega})H_{a2}(j\frac{\omega}{T_s})\Big[H_{ai}(j\frac{\omega+\omega_l}{T_s}) \\ &\quad \times F_{aa}(e^{j(\omega+\omega_l)}) + H_{ai}(j\frac{\omega-\omega_l}{T_s})F_{aa}(e^{j(\omega-\omega_l)})\Big] \\ &= M_2(\omega)e^{j\phi_2(\omega)}, \end{aligned} \tag{6}$$

and

$$\begin{aligned} M_m(\omega) &= \left|G_m(e^{j\omega})\right| \\ \phi_m(\omega) &= arg\left\{G_m(e^{j\omega})\right\}, \quad m = 1, 2. \end{aligned} \tag{7}$$

In order to simplify the expression, the fixed attenuation caused by interpolation and mixing in equations (5) and (6)

has been compensated. The final output of BI-DAS $Y(e^{j\omega})$ is obtained as follow

$$\begin{aligned} Y(e^{j\omega}) &= Y_1(e^{j\omega}) + Y_2(e^{j\omega}) \\ &= X(j\frac{\omega}{T_s})[G_1(e^{j\omega}) + G_2(e^{j\omega})] \\ &= X(j\frac{\omega}{T_s})T(e^{j\omega}), \end{aligned} \tag{8}$$

where $T(e^{j\omega})$ is the transfer function of the BI-DAS. Similar to (5) and (6), the final output of the BI-DAS in (8) can be written as

$$T(e^{j\omega}) = M_T(\omega)e^{j\phi_T(\omega)}, \tag{9}$$

where

$$M_T(\omega) = \sqrt{\begin{array}{l} M_1(\omega)^2 + M_2(\omega)^2 + \\ 2M_1(\omega)M_2(\omega)\cos\Delta\phi(\omega) \end{array}}, \tag{10}$$

$$\phi_T(\omega) = \arctan\frac{M_1(\omega)\sin\phi_1(\omega) + M_2(\omega)\sin\phi_2(\omega)}{M_1(\omega)\cos\phi_1(\omega) + M_2(\omega)\cos\phi_2(\omega)}, \tag{11}$$

and $\Delta\phi(\omega) = \phi_2(\omega) - \phi_1(\omega)$ is the PM between two sub-bands.

III. PROBLEM FORMULATION

A. DEFINITION OF OVERLAPPING BAND

Ideal analog filters have no transition region, which is impossible in practice. The overlapping frequency region exists between two adjacent sub-bands to some extent as illustrated in Fig. 2, where ω_{FCP} represents the intersection of two sub-bands. Signals with frequencies near ω_{FCP} will appear in both two sub-bands, simultaneously.

Signals with frequency ω_2 in Fig. 2, for example, belong to the second sub-band. However, due to the transition band of the first sub-band, the signals of this frequency don't get sufficient attenuation in the first sub-band, so that some signals still enter the first sub-band. Thus, the PM between two sub-bands in this frequency may cause signals that canceled or partially canceled to each other when signals are merged in the digital domain.

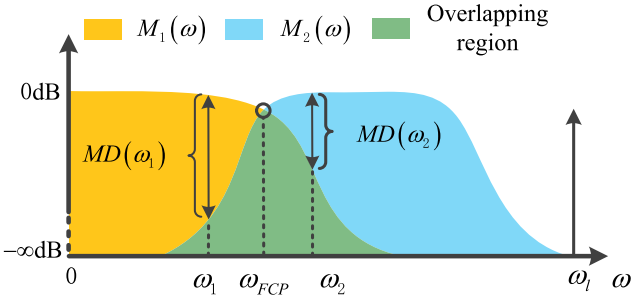

FIGURE 2. Magnitude-frequency response of $G_1(e^{j\omega})$ and $G_2(e^{j\omega})$ with overlapping region.

From a mathematical point of view, it can be seen from (10) and (11) that $M_T(\omega) \approx M_1(\omega)$ and $\phi_T(\omega) \approx \phi_1(\omega)$ when $M_1(\omega) \gg M_2(\omega)$ whatever the value of $\Delta\phi(\omega)$, vice versa. In order to weight the difference between $M_1(\omega)$ and $M_2(\omega)$, a variable $MD(\omega)$ is introduced as

$$MD(\omega) = 20 \times \log\frac{M_1(\omega)}{M_2(\omega)}. \tag{12}$$

According to (10), the maximum and minimum value of $M_T(\omega)$ is $M_1(\omega) + M_2(\omega)$ and $M_1(\omega) - M_2(\omega)$ corresponding to $\Delta\phi(\omega) = 0$ and $\Delta\phi(\omega) = \pm\pi$, respectively. Thus, the max magnitude fluctuation $MF(\omega)$ of $M_T(\omega)$ introduce by the PM is

$$\begin{aligned} MF(\omega) &= 20 \times \log\frac{M_1(\omega) + M_2(\omega)}{M_1(\omega) - M_2(\omega)} \\ &= 20 \times \log\frac{10^{\frac{MD(\omega)}{20}} + 1}{10^{\frac{MD(\omega)}{20}} - 1}. \end{aligned} \tag{13}$$

In (13), $MF(\omega)$ is a monotone decreasing function of $MD(\omega)$, which means that the magnitude response fluctuation of the sum of two sub-bands introduce by the PM would be negligible when $MD(\omega)$ is greater than a certain threshold. This threshold, namely MD_{max}, can be deduced by

$$MD_{max} = 20 \times \log\frac{10^{\frac{MF_{max}}{20}} + 1}{10^{\frac{MF_{max}}{20}} - 1}, \tag{14}$$

where MF_{max} depends on the compensation accuracy is the maximum acceptable fluctuation introduced by the PM of two sub-bands. From this perspective, the mathematical definition of the overlapping band can be written as

$$\begin{cases} X(j\frac{\omega}{T_s}) \in \textit{overlapping band } MD(\omega) \le MD_{max} \\ X(j\frac{\omega}{T_s}) \notin \textit{overlapping band } MD(\omega) > MD_{max}. \end{cases} \tag{15}$$

Above all, $M_T(\omega)$ whose ω is in the overlapping band is affected not only by the $M_1(\omega)$ and $M_2(\omega)$, but also by the $\Delta\phi(\omega)$. In contrast, the $M_T(\omega)$ whose ω is outside the overlapping band is only affected by the corresponding $M_1(\omega)$ or $M_2(\omega)$, and irrespective of the $\Delta\phi(\omega)$.

B. PHASE MISALIGNMENT IN THE OVERLAPPING BAND

After defining the overlapping band, this section focus on the impact of PM in the overlapping band. Assuming the ideal combined magnitude response of the overlapping band is $M_{ideal}(\omega) = M_1(\omega) + M_2(\omega)$, corresponding to $\Delta\phi(\omega) = 0$. The relative magnitude error $M_{rel}(\omega)$ introduced by $\Delta\phi(\omega)$ is defined as

$$M_{rel}(\omega) = 20 \times \log\frac{M_T(\omega)}{M_{ideal}(\omega)}, \omega \in \textit{overlapping band}. \tag{16}$$

Substituting (10) and (12) into (16), it can be reformed as

$$M_{rel}(\omega) = 10 \times \log\left(1 + \frac{2 \times 10^{\frac{MD(\omega)}{20}}(\cos\Delta\phi(\omega) - 1)}{(1 + 10^{\frac{MD(\omega)}{20}})^2}\right). \tag{17}$$

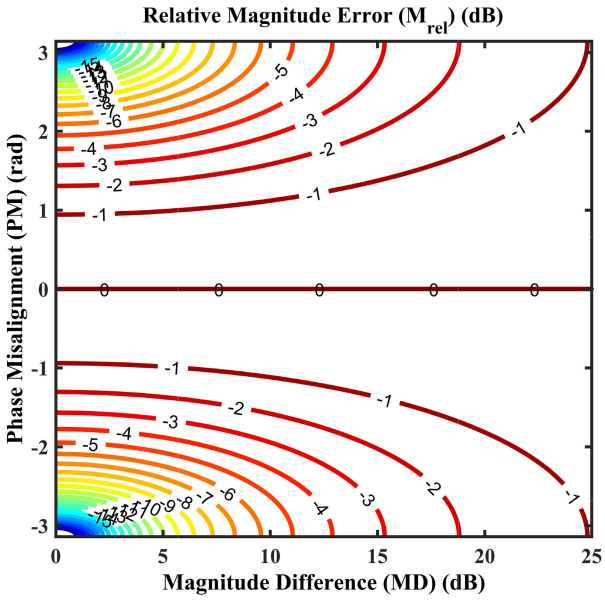

FIGURE 3. Contours of M_{rel} affected by MD and $\Delta\phi$ in the overlapping band.

Fig. 3 illustrates the contour of the M_{rel} in (17), when MD is constant, M_{rel} decreases with $\Delta\phi$ approaches $\pm\pi$. Especially for the case that $MD = 0$ and $\Delta\phi = \pm\pi$, the combined magnitude M_T is equal to zero, which leads a big dip in the combined magnitude response. Conversely, when $\Delta\phi$ is constant, M_{rel} is proportional to MD. In other words, the smaller the MD, the more sensitive the frequency point is to the change of $\Delta\phi$.

However, due to the non-linear phase response of analog filters $H_{a1}(j\Omega)$, $H_{a2}(j\Omega)$ and $H_{aa}(j\Omega)$, $G_1(e^{j\omega})$ and $G_2(e^{j\omega})$ also have non-linear phase response. Even though the digital filters $F_{aa}(e^{j\omega})$ and $F_{ai}(e^{j\omega})$ are linear-phase finite impulse response (FIR) filters. The non-linear phase response of $\phi_1(\omega)$ and $\phi_2(\omega)$ introduce the nonlinearity into the $\Delta\phi(\omega)$ between two sub-bands, which invalidates the linear PM correction method proposed in [9].

On the other hand, the different signal path in each sub-band introduces linear PM between two sub-bands. Therefore, $\Delta\phi$ in the overlapping band is denoted as a variable divided into two parts varies with ω

$$\Delta\phi(\omega) = -\overbrace{\omega \cdot \delta_d}^{linear\ phase} + \underbrace{\delta\phi(\omega)}_{non-linear\ phase}, \tag{18}$$

where δ_d is the group delay difference between two sub-bands, and $\delta\phi(\omega)$ is the non-linear PM between two sub-bands, which varies with ω.

IV. PROPOSED COMPENSATION STRATEGY

A. ESTIMATION OF THE MAGNITUDE AND PHASE DISTORTIONS

Prior to the compensation process, a simple estimation method based on sinusoidal signals is proposed for the magnitude difference and phase misalignment in the overlapping band.

First of all, a bunch of sinusoidal signals covers the entire bandwidth of the BI-DAS are fed into the system to determine the frequency range of the overlapping band in line accordance with (14) and (15).

After that, sinusoidal signals with N frequencies $(\omega_1, \omega_2, \ldots, \omega_N)$ evenly distributed in the overlapping band with the same amplitude are fed into the BI-DAS as excitations. Note that these signals should have sufficient amplitude so that they wouldn't drown into the background noise in each sub-band.

Adopting the sin-fitting algorithm [27], the magnitude distortion in ω_n, $(n = 1, 2, \ldots N)$ is calculated as

$$M_{rel}(\omega_n) = 20 \times \log\left(\frac{M_{absT}(\omega_n)}{M_{abs1}(\omega_n) + M_{abs2}(\omega_n)}\right) \tag{19}$$

according to (16), where $M_{abs1}(\omega_n)$, $M_{abs1}(\omega_n)$ and $M_{absT}(\omega_n)$ are the absolute magnitude of signals in each sub-band and combined output, respectively, and

$$\Delta\phi(\omega_n) = \phi_{abs2}(\omega_n) - \phi_{abs1}(\omega_n) \tag{20}$$

with $\phi_{abs1}(\omega_n)$ and $\phi_{abs2}(\omega_n)$ denoting the initial phase of signals in each sub-band. An average value of $\Delta\phi(\omega_n)$, $\Delta\bar{\phi}(\omega_n)$ is obtained after several measurements for the calculation of (20) and (21) to reduce the influence of the time jitter of the sampling clock and the phase jitter of the LO.

B. COMPENSATION MODULE

To compensate the PM in (18), the compensation module for PM is composed of three parts, as illustrated in Fig. 4, Integral Delay/Discard Module (IDM), Fractional Delay Module (FDM), and an APF $F_{ap}(e^{j\omega})$, where the IDM and FDM make up the linear compensation part of PM in (18). The combination delay of these two parts is denoted as $\hat{\delta}_d = \hat{\delta}_{Id} + \hat{\delta}_{Fd}$, where $\hat{\delta}_{Id}$ is an integer, and the IDM chooses whether Delay or Discard depends on the sign of $\hat{\delta}_{Id}$. An APF is adopted to compensate for the non-linear part of $\Delta\phi(\omega)$ in (18), since it significantly affects the phase response while the magnitude response is unity throughout the frequency band [10]. Suppose that the phase response characteristic of compensated signals in Fig. 4 is $\phi_{1c}(\omega)$, which is calculated as

$$\begin{aligned}\phi_{1c}(\omega) &= \phi_1(\omega) + \phi_c(\omega) \\ &= \phi_1(\omega) - \omega \cdot \hat{\delta}_d + \phi_{ap}(\omega),\end{aligned} \tag{21}$$

where $\phi_{ap}(\omega)$ is the phase response of $F_{ap}(e^{j\omega})$. The transfer function of a P-order APF based on cascading second-order

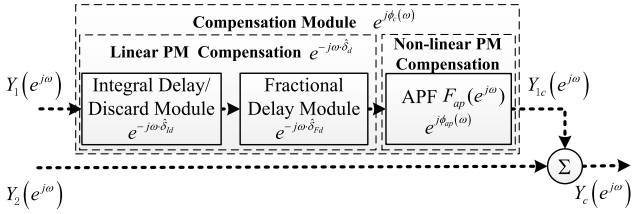

FIGURE 4. Compensation Module of the PM in the overlapping band.

sections, where P is an even number, in the Z domain is

$$F_{ap}(z)=\prod_{p=1}^{P/2}\frac{|\xi_p|^2-2\cdot\mathrm{Re}(\xi_p)\cdot z^{-1}+z^{-2}}{1-2\cdot\mathrm{Re}(\xi_p)\cdot z^{-1}+|\xi_p|^2\cdot z^{-2}} \tag{22}$$

where $\xi_p = M_p \cdot e^{j\theta_p}$ is a pole of the *pth* section, M_p and θ_p are the radii and angle of the ξ_p. Since the coefficients in (22) are all real, another pole of *pth* section is located at ξ_p^*, where $*$ is the conjugate operation. Therefore, the phase response of compensation module with a P-order APF is

$$\begin{aligned}\phi_c(\omega,\boldsymbol{U}) = &-(\hat{\delta_d}+P)\omega\\ &-2\sum_{p=1}^{P/2}\Bigg[\arctan\{\frac{M_p\sin(\omega-\theta_p)}{1-M_p\cos(\omega-\theta_p)}\}\\ &+\arctan\{\frac{M_p\sin(\omega+\theta_p)}{1-M_p\cos(\omega+\theta_p)}\}\Bigg]\end{aligned} \tag{23}$$

Note that the position of the compensation module depends on the definition of $\Delta\phi(\omega)$. In Fig. 4, the compensation module is added to the first sub-band since $\Delta\phi(\omega)$ is defined as $\phi_2(\omega)-\phi_1(\omega)$ in this paper. On the contrary, the compensation module should be added to another sub-band if $\Delta\phi(\omega) = \phi_1(\omega)-\phi_2(\omega)$. This alternative position allows the proposed strategy to be extended to BI-DASs with more than two sub-bands.

C. DESIGN ALGORITHM OF THE COMPENSATION MODULE

According to the analysis aforementioned, the phase response of the compensated first sub-band should satisfy that $\phi_{1c}(\omega)=\phi_2(\omega)$, which means

$$\begin{aligned}\Delta\bar{\phi}(\omega) &= \phi_c(\omega,\boldsymbol{U})\\ &= -(\hat{\delta_d}+P)\omega\\ &\quad -2\sum_{p=1}^{P/2}\Bigg[\arctan\{\frac{M_p\sin(\omega-\theta_p)}{1-M_p\cos(\omega-\theta_p)}\}\\ &\quad +\arctan\{\frac{M_p\sin(\omega+\theta_p)}{1-M_p\cos(\omega+\theta_p)}\}\Bigg].\end{aligned} \tag{24}$$

It is a typical nonlinear approximation problem for variable $\boldsymbol{U}$ in (24) that can be tackled using nonlinear optimization methods with nature. Define an error vector $\boldsymbol{R}$ as

$$\boldsymbol{R}=[e(\omega_1,\boldsymbol{U}),e(\omega_2,\boldsymbol{U}),\cdots,e(\omega_N,\boldsymbol{U})]^T, \tag{25}$$

with

$$e(\omega,\boldsymbol{U})=\sqrt{W(\omega)}\left[\phi_c(\omega,\boldsymbol{U})-\Delta\bar{\phi}(\omega)\right], \tag{26}$$

where $W(\omega)$ is the weighting function and

$$\boldsymbol{U}=\left[\hat{\delta}_d,\boldsymbol{M},\boldsymbol{\theta}\right], \tag{27}$$

and

$$\begin{aligned}\boldsymbol{M} &= \left(M_1,M_2,\cdots,M_{P/2}\right)^T\\ \boldsymbol{\theta} &= \left(\theta_1,\theta_2,\cdots,\theta_{P/2}\right)^T.\end{aligned} \tag{28}$$

According to the analysis in Section III-B, it is more sensitive to phase error where the amplitude deviation between two sub-bands $MD(\omega)$ is small, so that the weighting function $W(\omega)$ in this situation is defined as

$$W(\omega)=10^{-MD(\omega)/1000}. \tag{29}$$

The weighted least square (WLS) problem in this paper can be described as

$$\begin{aligned}&\text{Minimize } E(\boldsymbol{U})=\frac{1}{N}\boldsymbol{R}^T\boldsymbol{R}\\ &\text{Subject to } M_p<1,\quad p=1,2,\cdots,P/2,\end{aligned} \tag{30}$$

where the constrain of M_p<1 is used to guarantee the stability of the designed filter $F_{ap}(z)$ [10].

To solve the WLS problem in (29), this section provides a novel weighted HPSOLM algorithm. In this algorithm, PSO is firstly utilized to find the near-optimal point in the global space. Then the LM algorithm is followed to find the local-optimal based on the near-optimal point calculated by the PSO.

1) PARTICLE SWARM OPTIMIZATION ALGORITHM

The PSO algorithm [28] is a population-based multipoint evolutionary algorithm. The searching process in PSO starts with a population of particles move in a search space by following the current optimum particles and changing their positions and velocity to find the best particle position. During its movement, particles distribute information among them to search in a good area of the search space. The associated velocity of an individual particle in $\boldsymbol{U}_s$ is

$$\begin{aligned}\boldsymbol{V}_s^{k+1} = \boldsymbol{V}_s^k &+ C_1\cdot r_1\cdot\left(\boldsymbol{zb}_s-\boldsymbol{U}_s^k\right)\\ &+ C_2\cdot r_2\cdot\left(\boldsymbol{gb}-\boldsymbol{U}_s^k\right),\end{aligned} \tag{31}$$

where $s\in[1,S]$ represents the index of population of particles and corresponding velocity matrix, where S is the population size of particles, C_1, and C_2 are acceleration constants, r_1, r_2 are uniformly distributed random number in [0, 1], $\boldsymbol{zb}_s$ and $\boldsymbol{gb}$ are the local best solutions and global best solution, and $k\in[1,K]$ is the iteration index, where K is the maximum iteration times of PSO. The population is updated as

$$\boldsymbol{U}_s^{k+1}=\chi\left\{\boldsymbol{U}_s^k+\boldsymbol{V}_s^{k+1}\right\}, \tag{32}$$

where $\chi\{\cdot\}$ is a constraining factor, which guarantees the stability of the APF. The necessary and sufficient condition for stability of APFs is that all the poles are in the unit circle [10], corresponding to M_p<1, $p=1,2,\cdots,P/2$. Since $M_p=1$ is critically stable, a variable ρ slightly less than 1 is introduced to guarantee the stability of APF. The designed APF is stable whose M_p is less or equal to ρ, which can be used as a constrained factor of the population in PSO

$$\chi\{\boldsymbol{U}_s\}=\begin{cases}\boldsymbol{U}_s\cdot M_p=\rho\boldsymbol{U}_s\cdot M_p>\rho\\ \boldsymbol{U}_s\cdot M_p=\boldsymbol{U}_s\cdot M_p\,\boldsymbol{U}_s\cdot M_p\le\rho\end{cases} \tag{33}$$

After a new population is formed, the greedy based selection procedure is introduced for sorting and updating of $\boldsymbol{zb}_s$ and $\boldsymbol{gb}$.

2) PARAMETERIZED LEVENBERG-MARQUARDT ALGORITHM

The final $\boldsymbol{gb}$ of PSO algorithm is substituted into the LM [15] algorithm as the initial condition. However, utilizing the LM algorithm directly on the $\boldsymbol{gb}$ may cause M_p to exceed the stable interval of the APF in the compensation module during the iteration process since the LM algorithm is a kind of unstrained optimization method.

Inspired by [29], if

$$M_p = F(x_p) = \frac{\rho}{1 + e^{-x_p}}, \tag{34}$$

then M_p varies over the interval $0<M_p<\rho$ when the parameter x_p varies from $-\infty$ to ∞. Besides, (34) is a monotonically increasing function, which provides a one-to-one mapping between the entire space and the stability region of the APF in the compensation module, as illustrated in Fig. 5.

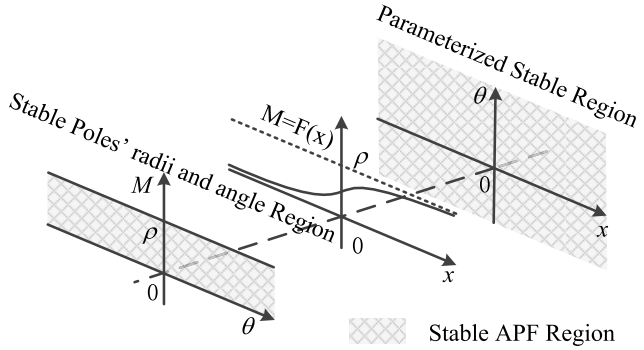

FIGURE 5. Parameterizing process constrained optimization problem to unconstrained optimization problem.

In (23), it is a periodic function for θ_p whose period is 2π. So that there is no constrain on the θ_p, so as to the $\hat{\delta}_d$. Thus, the constrained WLS problem in (30) is transformed into an unconstrained WLS problem

$$\text{Minimize} \quad E(\hat{\boldsymbol{U}}) = \frac{1}{N}\boldsymbol{R_x}^T\boldsymbol{R_x}, \tag{35}$$

where

$$\boldsymbol{R_x} = \left(e_x(\omega_1, \hat{\boldsymbol{U}}), e_x(\omega_2, \hat{\boldsymbol{U}}), \cdots, e_x(\omega_N, \hat{\boldsymbol{U}})\right)^T, \tag{36}$$

with

$$e_x(\omega, \hat{\boldsymbol{U}}) = \sqrt{W(\omega)}(\phi_c(\omega, \hat{\boldsymbol{U}}) - \Delta\bar{\phi}(\omega)), \tag{37}$$

and

$$\begin{aligned}\phi_c(\omega, \hat{\boldsymbol{U}}) = &-(\hat{\delta_d} + P)\omega \\ &- 2\sum_{p=1}^{P/2}\left[\arctan\{\frac{F(x_p)\sin(\omega - \theta_p)}{1 - F(x_p)\cos(\omega - \theta_p)}\}\right. \\ &\left. + \arctan\{\frac{F(x_p)\sin(\omega + \theta_p)}{1 - F(x_p)\cos(\omega + \theta_p)}\}\right],\end{aligned} \tag{38}$$

$$\begin{aligned}\hat{\boldsymbol{U}} &= \left[\hat{\delta}_d, \boldsymbol{X}, \boldsymbol{\theta}\right] \\ \boldsymbol{X} &= \left(x_1, x_2, \cdots, x_{P/2}\right)^T,\end{aligned} \tag{39}$$

with $-\infty<x_p, \theta_p, \hat{\delta}_d<\infty$ characterizing all the compensation module with stable APF where parameters can take any values in the entire parameter space.

Thus, the (30) can be tackled by the LM algorithm without losing the stability of APF filters. The LM algorithm has a strong ability to find a local optimistic result, whose updating vector Δ is obtained by

$$\boldsymbol{\Delta} = (\boldsymbol{H} + \lambda\boldsymbol{D})^{-1}\boldsymbol{J}^T\boldsymbol{W}\boldsymbol{R}, \tag{40}$$

where

$$\boldsymbol{H} = \boldsymbol{J}^T\boldsymbol{W}\boldsymbol{J},$$

is the approximate Hessian matrix,

$$\boldsymbol{D} = \text{diag}\left\{\boldsymbol{H}\right\}, \boldsymbol{W} = \text{diag}\left\{W(\omega_1), W(\omega_2), \cdots, W(\omega_N)\right\}$$

are diagonal matrix contains all the diagonal elements of $\boldsymbol{H}$ and the weighting matrix whose diagonal elements are $\{W(\omega_1), W(\omega_2), \cdots, W(\omega_N)\}$ with off-diagonal elements are all zeros, respectively.

In (40), $\boldsymbol{J}$ is the Jacobin matrix of (38). LM algorithm switches between gradient descent method (GDM) and the Gauss-Newton method (GNM) by controlling parameter λ, which determines how the LM algorithm works and has a great initial value. If the current E error is smaller than the last time, then λ becomes smaller, the algorithm is switched to the approximate GNM. Otherwise, reject this iteration process, λ is increased more like a GDM. It recalculates $\boldsymbol{\Delta}$ until the E goes down. The integrated HPSOLM algorithm proposed is summarized in **Algorithm** 1.

The proposed algorithm makes use of the global search capability of the PSO algorithm and overcomes the defect of local optimization and initial value selection of the LM algorithm. Meanwhile, the introduction of the LM algorithm overcomes the shortcoming of the PSO algorithm that the optimization ability declines near the global minimum, which further guarantees the numerical stability of the algorithm while improving the accuracy of the algorithm without losing the stability of the APF in the compensation module.

D. PARAMETER SELECTION

In **Algorithm** 1, parameters $\boldsymbol{S}$, $\boldsymbol{C_1}$, $\boldsymbol{C_2}$, and $\boldsymbol{K_{PSO}}$ will affect the global search ability of the HPSOLM algorithm. $\boldsymbol{C_1}$ and $\boldsymbol{C_2}$, corresponding to cognitive and social ratio of the PSO algorithm are set to $\boldsymbol{C_1} = \boldsymbol{C_2} = 2$ as previous lecture [30]. Higher $\boldsymbol{S}$ and $\boldsymbol{K_{PSO}}$ value means better global optimization ability of the HPSOLM algorithm, which may also increase the execution time of the optimization process. In the proposed HPSOLM algorithm, the parameters $\boldsymbol{S}$ is suggested around 100 in this paper, since the problem to be solved is a highly nonlinear complex problem [31]. $\boldsymbol{K_{LM}}$ determines the local search ability of the HPSOLM algorithm. Due to the LM is a local search algorithm, it should not be set too large.

Algorithm 1 Hybrid PSO-LM Algorithm

Setting: $S, C_1, C_2, K_{PSO}, K_{LM}, \rho$
Initialization: Generating random U_s with size S
  PSO ALGORITHM: $k = 1$
  while k<K_{PSO} **do**
    for s=1:S **do**
      $V_s^{k+1} = V_s^k + C_1 \cdot r_1 \cdot (zb_s - U_s^k) + C_2 \cdot r_2 \cdot (gb - U_s^k)$
      $U_s^{k+1} = \chi\{U_s^k + V_s^{k+1}\}$
      if $E(U_s^{k+1})$<$E(zb_s)$ **then**
        $zb_s = U_s^{k+1}$
      end if
      if $E(U_s^{k+1})$<$E(gb)$ **then**
        $gb = U_s^{k+1}$
      end if
    end for
    $k = k + 1$;
  end while
  Switching to the LM algorithm,
  $k = 1, \lambda = 10000, v = 10$
  Parameterizing gb **to** $\hat{U}_1$**,**
  $\hat{U}_1 \cdot x_p = F^{-1}(gb \cdot M_p), p = 1, 2, \cdots, P/2$
  while k<K_{LM} **do**
    $H_k = J_k^T W J_k, D_k = \text{diag}\{H_k\}$
    $\Delta_k = (H_k + \lambda \cdot D_k)^{-1} J_k \cdot W \cdot {R_x}^k$
    $\hat{U}_{new} = \hat{U}_k + \Delta_k$
    if $E(\hat{U}_{new})$<$E(\hat{U}_k)$ **then**
      $\hat{U}_{k+1} = \hat{U}_{new}$
      $\lambda = \lambda/10$
      $v = 10$
    else
      $\hat{U}_{k+1} = \hat{U}_k$
      $\lambda = v \times \lambda$
      $v = 10 \times v$
    end if
    $k = k + 1$;
  end while

For multi-modal problems, once it falls into the local optimal, increasing the number of iterations is useless for jumping out the local optimal. The selection of K_{LM} and K_{PSO} are according to the specific problem, which will be discussed in Section VI.

E. COMPUTATIONAL COMPLEXITY

The computational complexity of the proposed HPSOLM algorithm is the sum of the PSO and the LM algorithm, which are $K_{PSO} \times S \times \mathcal{O}(h)$ and $K_{LM} \times \mathcal{O}(h^3)$, respectively, where h is the number of the coefficients to be solved [32], [33].

Assuming that K_{PSO}, K_{LM} and S are held unchanged, the computational complexity of the LM algorithm in the HPSOLM algorithm is lower than that of the PSO algorithm when h is small. So that, the computational complexity of the HPSOLM algorithm is less than that of the conventional PSO algorithm under the same condition, whose iterations are $K'_{PSO} = K_{PSO} + K_{LM}$.

The complexity of the LM algorithm will exceed that of the PSO algorithm with the increased h. Meanwhile, the complexity of the HPSOLM algorithm will be higher than the conventional PSO algorithm with the same iterations. However, due to the randomness of the PSO algorithm, multiple operations may be required to obtain the optimal value. In contrast, the HPSOLM algorithm can get the optimal solution without numerous runs. From this perspective, the HPSOLM algorithm still has lower computational complexity than the conventional PSO algorithm.

V. IMPLEMENTATION PLATFORM

The proposed compensation module has been implemented in an BI-DAS with 20Gsps sampling rate and 5.5GHz bandwidth, whose main circuit diagram is illustrated in Fig. 6. In this implementation platform, signals from RF generator (SMB100A, R&S, Inc.) are fed into a splitter which splits the RF signals into two identical signals.

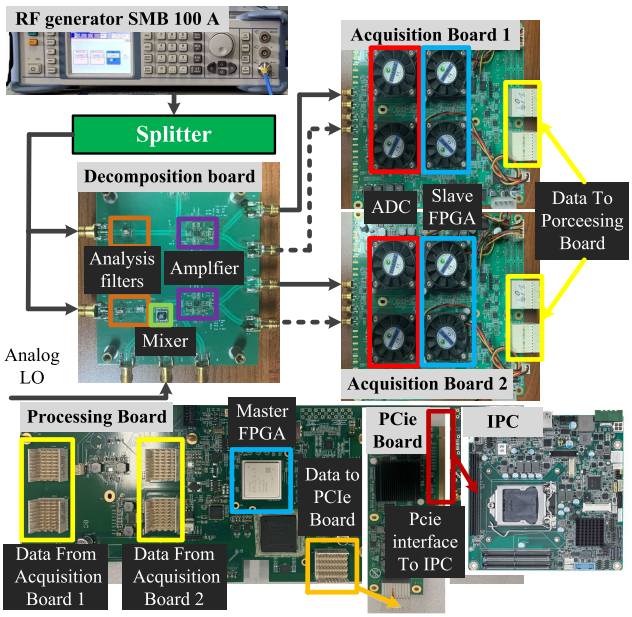

FIGURE 6. Implementation platform of BI-DAS in this paper.

The split signals are decomposed into two frequency sub-bands, where the high-frequency sub-band is down-converted by analog mixer through the decomposition board. In the decomposition board, the -3db bandwidth of analysis filters $H_{a1}(j\Omega)$ and $H_{a2}(j\Omega)$ are 3400MHz and {3400MHz, 5500MHz}, respectively. The frequency of the analog LO, Ω_l is chose as 6000MHz. Decomposed signals are converted to differential signals via an ultra-wideband amplifier.

Signals of two sub-bands converted into differential form are fed into two acquisition boards. Each acquisition board is composed of two ADC (EV10AQ190, TELEDYNE E2V, Inc.) with 5Gsps sampling rate, 10bit quantization bit, corresponding slave Field Programmable Gate Array

(FPGA, XC7K325T, Xilinx, Inc.) used for the data receiving and controlling of each ADC. The two ADCs in an acquisition board work in time-interleaved (TI) manner to achieve a sampling rate of 10Gsps, which is the sampling rate for each sub-band. The track-and-holds of ADCs play the role of anti-aliasing filters $H_{aa}(j\Omega)$ in this platform, whose -3dB bandwidth is 3400MHz. Note that the errors introduced by TI-ADC have been corrected, which are not considered in the following experiments.

The slave FPGA corresponding to each acquisition board's ADC receives the sampled data and transmits it to the master FPGA (XC7K325T, Xilinx, Inc.) on the processing board through the CPCI connector for data combination of TI-ADC, so as to recover the data stream of 10Gsps sampling rate. After completing the combination of TI-ADC, the data is sent to industry personal computer (IPC) via a peripheral component interface express (PCI-e) interface for subsequent digital signal processing. All the signal processing processes in the experiment were realized in MATLAB 2016A in IPC with an Intel Core I7-6700 3.4 GHz CPU and 8 GB RAM.

In the digital signal processing section, the pass-band and stop-band cutoff numerical frequencies of the anti-aliasing filter $F_{ai}(e^{j\omega})$ are 0.45π and 0.50π, respectively. The pass-band and stop-band cutoff numerical frequencies of the anti-image filter $F_{aa}(e^{j\omega})$ are 0.55π and 0.60π, respectively. These filters are all linear phase low-pass FIR filters whose orders are 163, pass-band fluctuation is less than 0.01dB, stop-band attenuation is greater than 80dB. In order to ensure the accuracy of estimation and compensation of the overlapping band, the linear delay introduced by these FIR filters has been compensated by discarding points. The parameters of the experimental platform are summarized in Table 1.

TABLE 1. Parameter value of the implementation platform.

Parameter	Value
Sampling rate of each sub-bands (Gsps)	10
Number of sub-bands	2
bandwidth (-3dB) of $H_{a1}(j\Omega)$ (MHz)	DC-3400
bandwidth (-3dB) of $H_{a2}(j\Omega)$ (MHz)	3400-5500
bandwidth (-3dB) of $H_{aa}(j\Omega)$ (MHz)	DC-3400
Frequency of the LO (MHz)	6000
pass-band cut-off frequency of $F_{aa}(e^{j\omega})$	0-0.45pi
stop-band cut-off frequency of $F_{aa}(e^{j\omega})$	0.5pi
pass-band cut-off frequency of $F_{ai}(e^{j\omega})$	0,0.55pi
stop-band cut-off frequency of $F_{ai}(e^{j\omega})$	0.6pi
digital filter orders	163
pass-band ripples (dB)	0.01
stop-band attenuation (dB)	80

VI. RESULTS AND DISCUSSION

In this section, the proposed compensation module and HPSOLM algorithm are validated based on the platform in Section V. The overlapping band is determined by a bunch of equal amplitude sinusoidal signals, with equal frequency interval 10 MHz around the 3400MHz, generated from the SMB 100A RF generator.

Taking the method proposed in Section IV-A, the measured magnitude response and phase misalignment $\Delta\bar{\phi}$ with 100 times average processing is illustrated in Fig. 7 below. The maximum fluctuation MF_{max} in this experiment is set as $0.1\,dB$, which means that the overlapping band, according to (15), is the frequency band whose $MD(\omega) \leq 44\,dB$, corresponding to the frequency from 3210 MHz to 3780 MHz. Since the signals path of the second sub-band is longer than the first sub-band, the overall trend of the measured $\Delta\bar{\phi}(\omega)$ is decreasing. Note that the magnitude of signals with 3210 MHz frequency is normalized to 0dB as a reference.

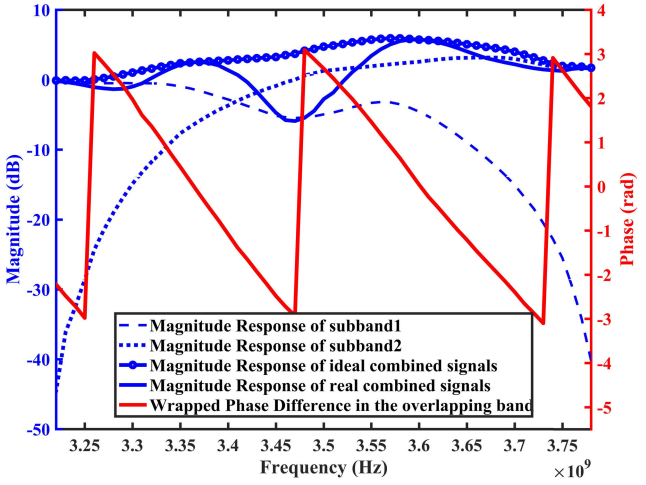

FIGURE 7. Measured magnitude response and phase misalignment in the overlapping band based on the platform in Section V with 100 times average processing.

In Fig. 7, there is a great dip of real combined signals compared with ideal combined signals between 3400 MHz to 3550MHz, where the phase misalignment $\Delta\bar{\phi}(\omega)$ is around $\pm\pi$. However, when the $MD(\omega)$ between two sub-bands is sufficiently large, the $M_{rel}(\omega)$ is small even though the $\Delta\bar{\phi}(\omega)$ is around $\pm\pi$, which confirms the analysis in Section III.B.

Following the definition of the overlapping band, the compensation strategy proposed is adopted for the compensation of the $\Delta\phi(\omega)$. As a reference, PSO algorithm is selected for comparison. The parameters setting of the HPSOLM and PSO algorithm are listed in Table 2, where the PSO algorithm's parameters have the same value in both HPSOLM and PSO algorithm. Meanwhile, the mean and statistical values are adopted within 100 independent runs. In the initialization process of the PSO algorithm, the range of the random population is

$$\begin{cases} \boldsymbol{U}_s \cdot M_p & \in [0,\ \rho] \\ \boldsymbol{U}_s \cdot \theta_p & \in [0,\ 2\pi] \\ \boldsymbol{U}_s \cdot \hat{\delta}_d^p & \in \begin{bmatrix} \boldsymbol{Min}\left\{\delta_{gd}(\omega)\right\} - P, \\ \boldsymbol{Max}\left\{\delta_{gd}(\omega)\right\} - P \end{bmatrix}. \end{cases} \tag{41}$$

TABLE 2. Parameter setting of the PSO and the HPSOLM algorithm.

Algorithm	Parameters						
	S	P	C_1	C_2	ρ	K_{PSO}	K_{LM}
HPSOLM	128	2	2	2	0.98	500	500
PSO	128	2	2	2	0.98	1000	-

In (41), $\delta_{gd}(\omega)$ is the group delay of $\Delta\bar{\phi}(\omega)$, whose maximum and minimum value are 66.88 and 101.90 in this experiment, respectively.

The IDM and FDM in the proposed compensation module in these experiments are realized by adding zeros before the data and a FIR based fractional delay filter with 51 orders, respectively.

A. COMPENSATION PERFORMANCE

Results below are obtained by taking the average over 100 independent runs to reduce the randomness of the PSO algorithm. Fig. 8 visualizes the contrast of PM in the overlapping band with compensation module (CM) designed by the PSO algorithm and HPSOLM algorithm. The compensated PM of the proposed HPSOLM is closed to zeros than the conventional PSO method, at the same number of iterations, especially in the frequency at which the $MD(\omega)$ between the two sub-bands is small (ω from 1.059 to 1.096 rad), corresponding to the high weighting function value.

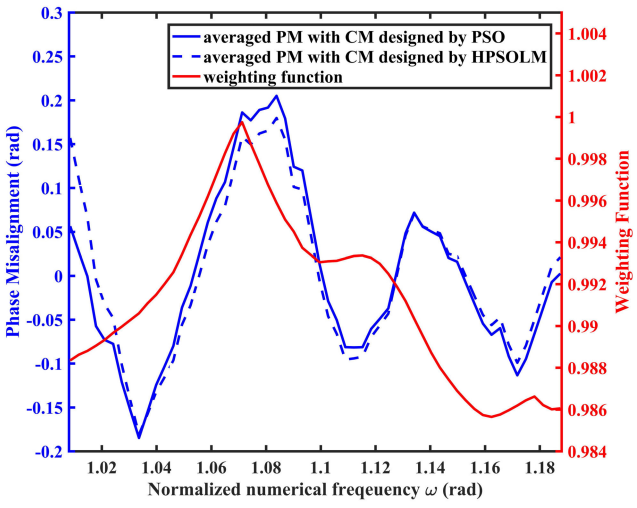

FIGURE 8. Compensated phase misalignment comparison between PSO and HPSOLM algorithm.

Although the compensation results of HPSOLM algorithm are worse than the conventional PSO algorithm when the ω is less than 1.02 rad. The $M_{rel}(\omega)$ is insensitive to the PM where $MD(\omega)$ is bigger, corresponding to the low weighting function in this frequency band, so it has little impact on the compensation result and can be ignored.

Fig. 9 shows the $M_{rel}(\omega)$ before and after the proposed compensation module, where the $M_{rel}(\omega)$ is greatly reduced

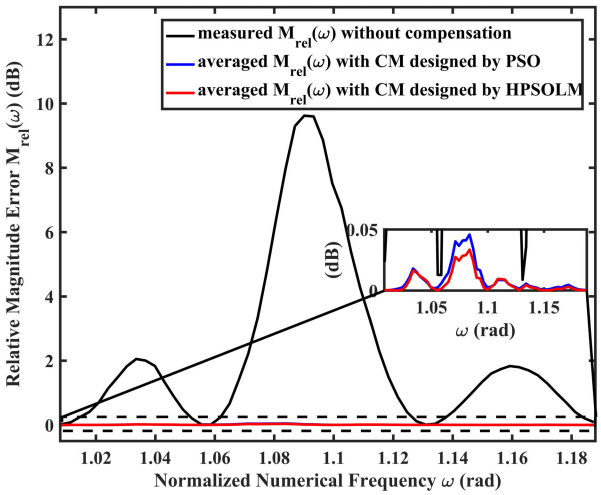

FIGURE 9. Relative Magnitude Error $M_{rel}(\omega)$ comparison with and without compensation module.

blow 0.1dB (maximum tolerable fluctuation within an overlapping band, definition of the overlapping band) after the compensation module designed by both PSO and HPSOLM. However, referring to the zoom figure in Fig. 9, the compensated $M_{rel}(\omega)$ with compensation module designed by the proposed HPSOLM algorithm has a better compensation effect than those designed by the conventional PSO algorithm, especially in the ω from 1.059 to 1.096 rad.

B. CONVERGENCE PERFORMANCE

This part compares the convergence curves of PSO and HPSOLM implementations in Section VI-A, whose results are shown in Fig. 10. In these implementations, the PSO algorithm has a slow convergence rate in the whole process. However, the HPSOLM uses the PSO algorithm to perform a coarse search in the solution space at the first 500 iterations,

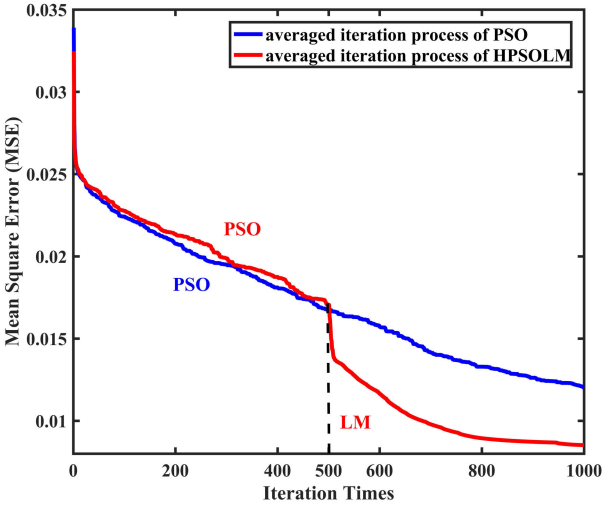

FIGURE 10. Iteration process comparison between PSO and HPSOLM algorithm.

and then uses fine searchability of the LM algorithm to speed up the convergence. LM algorithm accelerates the speed of convergence, which makes the hybrid algorithm to obtain better accuracy than the conventional PSO algorithm in the same number of iterations, where the averaged final result of HPSOLM drops from 0.012 to 0.0085 within 1000 iterations.

C. STABILITY PERFORMANCE

Fig. 11 and Fig. 12 show the poles and zeros location of the APF in compensation module design by PSO and HPSOLM within 100 independent runs, respectively. The poles of each run are in the unit circle for APFs designed by both PSO and HPSOLM, illustrated in the zoomed detail in Fig. 11 and Fig. 12, which confirms the stability of these filters. Especially for the HPSOLM, despite the unconstrained optimization approach, due to the mentioned parameterizing operation in Section IV-C2, the stability of these filters is still guaranteed.

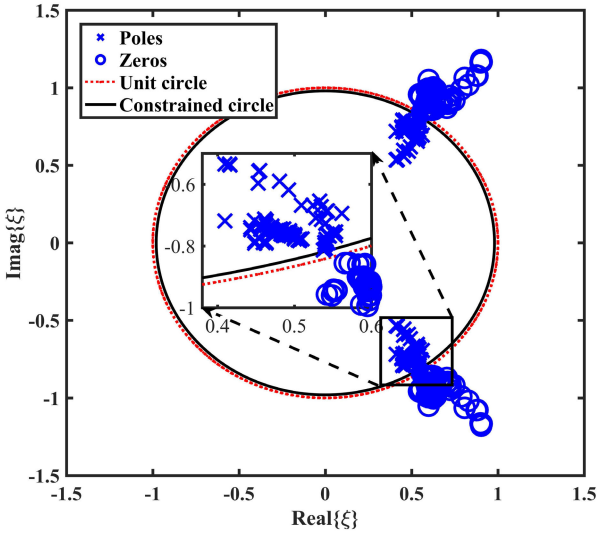

FIGURE 11. Poles and zeros iteration result of PSO within 100 independent runs.

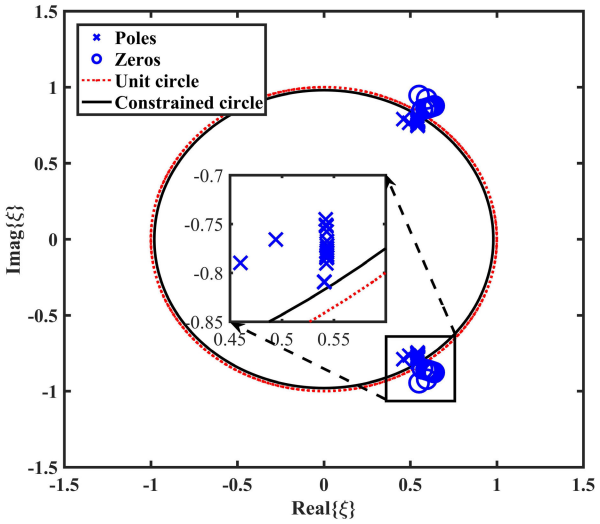

FIGURE 12. Poles and zeros iteration result of HPSOLM within 100 independent runs.

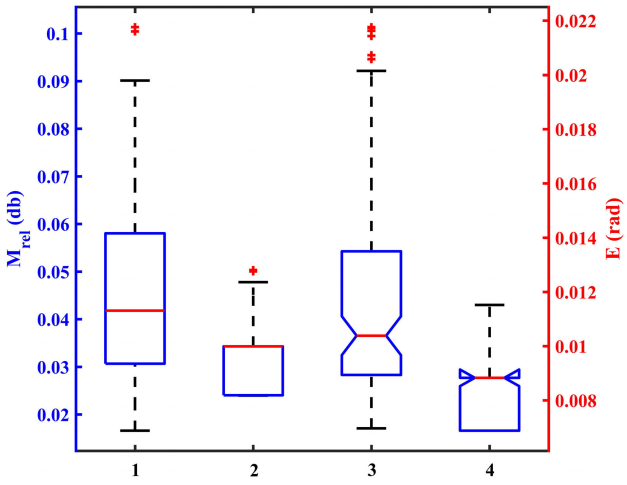

FIGURE 13. Static performance of PSO and HPSOLM algorithm in 100 independent runs (1 and 3, M_{rel} and E of 1000 times PSO with 128 popsize; 2 and 4, M_{rel} and E of 500 times PSO with 128 popsize and 500 times LM).

D. STATIC PERFORMANCE

To verify the efficiency of the proposed HPSOLM algorithm, this section discusses the static performance comparison between the PSO and HPSOLM algorithm within 100 independent runs, which is illustrated in Fig. 13. According to the whisker plot in Fig. 13, the median value for maximum M_{rel} is reduced from 0.042 dB to 0.034 and the median value of phase MSE is reduced from 0.0104 rad to 0.0088 rad for PSO and HPSOLM algorithm, respectively.

Besides, the results of HPSOLM have high concentration than those of PSO. The high concentration performance is consistent with the experiment in Fig. 11 and 12, where the poles and zeros location of APF designed by the HPSOLM is more concentrated than those designed by the PSO algorithm. Further more, there are some M_{rel} of the PSO algorithm exceed the 0.1 dB, which invalidates the compensation process.

Table 3 lists the time elapse comparison between conventional PSO and HPSOLM algorithm. Compared with the conventional PSO algorithm, the introduction of the LM

TABLE 3. Time elapse static performance of PSO and HPSOLM algorithm.

Performance		Algorithm	
		PSO	HPSOLM
Time Elapse (s)	Max	8.1141	**4.5906**
	Min	6.8626	**3.3491**
	Mean	7.5396	**3.8274**

algorithm not only speeds up the rate of convergence but also overcomes the randomness of the PSO algorithm's results. The HSPOLM algorithm can get the optimal result after one iteration process, instead of multiple iteration process to get the optimal result like PSO, which reduces the complexity of designing compensation module to some extent. Also, the HPSOLM algorithm consumes less time than the PSO algorithm in the same number of iterations under the setting in Table 2.

E. DISCUSSION

The experiments in this section discuss the impact of the PSO and LM algorithm on the proposed HPSOLM algorithm. Referring to the description in Section IV-C, the PSO algorithm is used for global search in the entire space, while the LM focuses on locating the best solution start from the results of the PSO algorithm.

Fig. 14 shows the iteration results with various iteration times of the LM algorithm after an iteration results of the PSO algorithm with 500 iteration times. It can be seen that the final iteration results of the hybrid algorithm will converge further with the increase of the number of the LM algorithm iterations. However, the gain of iteration's number on the convergence of the final result is weakened when the number of iterations of the LM algorithm is greater than 500. For non-quadratic and multi-modal problems, the PSO algorithm has a certain probability falling into the region around the local optimal solution, whereas the LM algorithm can only iterate to the local optimal solution starting from these initial points. Even if the number of the LM algorithm iteration increases, the local optimal solution cannot be jumped out to the global optimal solution.

To verify this problem, another experiment is designed with constant iteration times of LM and various iteration

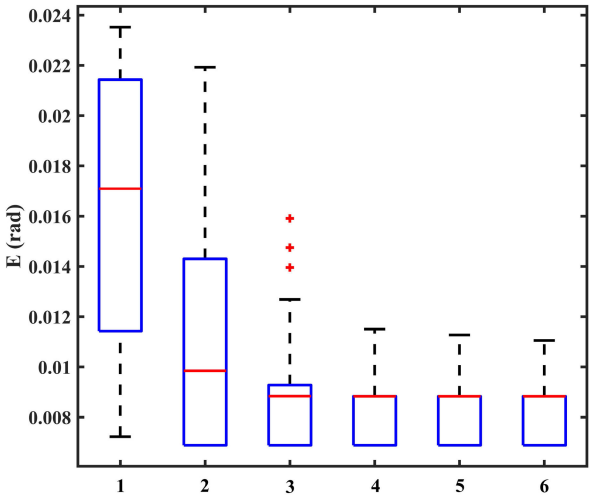

FIGURE 14. Iteration results of HPSOLM with constant times of PSO and various times of LM in 100 independent runs. (1, 128 popsize with 500 times PSO. 2-6, 128 popsize with 500 times PSO and 100, 300, 500, 700, 900 times LM;).

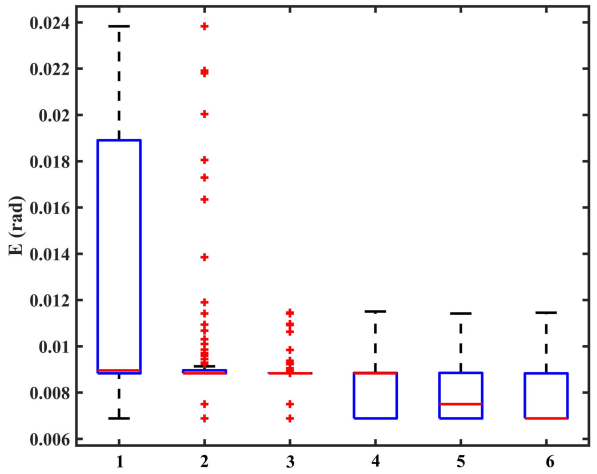

FIGURE 15. Iteration results of HPSOLM with constant iteration times of LM and various PSO in 100 independent runs. (1-5, 128 popsize with 500 times LM and 100, 300, 500, 700, 900 times PSO; 6, 256 popsize with 900 times PSO and 500 times LM).

times of PSO algorithm. In Fig. 15, when the number of PSO iterations is small, such as 100 iteration times, the hybrid algorithm is degenerated to a random LM algorithm, the global search ability is reduced, and a large number of iteration results remain in the local optimal solution.

With the increase of the PSO iterations' times, the global optimization ability of the algorithm is enhanced. The algorithm can escape out of partial local optimization, and the final result of the algorithm is improved, illustrated in 2 to 5 in Fig. 15. These show that the global search ability of the hybrid PSO algorithm is positively correlated with the iteration number of PSO. In addition, under the same number of iterations, increasing the population number of PSO can also enhance the global search ability of the hybrid algorithm. The medium value of 6 is reduced to 0.0069 from 0.0075 in 5, as shown in Fig. 15

According to the above experiments, in the HPSOLM algorithm, the PSO algorithm determines the global search capability of the HPSOLM algorithm. In contrast, the LM algorithm determines the local optimal search capability of the HPSOLM algorithm.

Therefore, in the HPSOLM algorithm, the global search ability should be guaranteed, that is, PSO should have sufficient iterations or the population size. However, increasing the number of iterations and the population size of the PSO algorithm will undoubtedly increase the consumption of time elapse. Therefore, a compromise scheme should be selected according to specific problems when utilizing the HPSOLM algorithm.

VII. CONCLUSION AND FUTURE WORK

This paper devotes to the phase misalignment of the overlapping bands in BI-DASs. The mathematical definition of the overlapping band is given by analyzing the influence of phase misalignment in the overlapping band. On this basis, a com-

pensation module with an all-pass filter is proposed, which divides the phase misalignment into linear and non-linear parts and compensates them, respectively. An HPSOLM algorithm is proposed to design the compensation module, which combines the PSO algorithm with the LM algorithm. Parameterizing the pole position of the all-pass filter before utilizing the LM avoids the problem that the unconstrained optimization method may cause the instability of the all-pass filter in the compensation module. Experimental results show that the proposed compensation module effectively compensates the phase misalignment and the proposed HPSOLM algorithm has better effectiveness than the conventional PSO algorithm on the premise of ensuring the stability of designed APF while less time elapse.

Since the proposed HPSOLM algorithm is based on the PSO algorithm, it inherits some shortcomings of the PSO algorithm, such as the premature problem, especially when the problem dimension is large. In the following works, the authors will focus on other swarm intelligence algorithms, such as the Firefly Search algorithm, Cuckoo Search algorithm, Beetle Antennae Search algorithm, etc., which may have the potential to provide more excellent optimization results.

REFERENCES

[1] M. H. Eissa, A. Awny, M. Ko, K. Schmalz, M. Elkhouly, A. Malignaggi, A. C. Ulusoy, and D. Kissinger, "A 220–275 GHz direct-conversion receiver in 130-nm SiGe: C BiCMOS technology," *IEEE Microw. Wireless Compon. Lett.*, vol. 27, no. 7, pp. 675–677, Jul. 2017.

[2] A. Eecs, "Time-domain ultra-wideband synthetic imager in silicon," in *Proc. Int. Conf. IEEE Eng. Med. Biol. Soc. (Embc)*, 2011.

[3] A. Sureka, P. J. Pupalaikis, B. Yamrone, R. Delbue, A. S. Khanna, K. Doshi, and B. Bhat "Technologies for very high bandwidth real-time oscilloscopes," in *Proc. IEEE Bipolar/BiCMOS Circuits Technol. Meeting (BCTM)*, Sep./Oct. 2014, pp. 128–135.

[4] P. Pupalaikis, "An 18 GHz bandwidth, 60 GS/s sample rate real-time waveform digitizing system," in *IEEE MTT-S Int. Microw. Symp. Dig.*, Jun. 2007, pp. 195–198.

[5] J. Song, S. Tian, L. Guo, and K. Yang, "Digital correction of frequency-response errors in bandwidth-interleaved ADCs," *Electron. Lett.*, vol. 52, no. 19, pp. 1596–1598, Sep. 2016.

[6] J. Song, S. Tian, and Y.-H. Hu, "Analysis and correction of combined channel mismatch effects in frequency-interleaved adcs," *IEEE Trans. Circuits Syst. I, Reg. Papers*, vol. 66, no. 2, pp. 655–668, Feb. 2019.

[7] J. Song, S. Tian, Y.-H. Hu, and P. Ye, "Digital iterative harmonic rejection and image cancellation for LPF-less frequency-interleaved analog-to-digital converters," *IEEE Trans. Circuits Syst. II, Exp. Briefs*, vol. 66, no. 12, pp. 2072–2076, Dec. 2019.

[8] D. G. Knierim, "Test and measurement instrument including asynchronous time-interleaved digitizer using harmonic mixing," Tech. Rep., 2014.

[9] A. Tumewu, K. Miyazawa, T. Aoki, T. J. Yamaguchi, K. Degawa, and T. Akita, "Phase-based alignment of two signals having partially overlapped spectra," in *Proc. IEEE Int. Conf. Acoust., Speech Signal Process.*, Apr. 2009, pp. 3337–3340.

[10] A. Antoniou, *Digital Filters: Analysis, Design and Applications: Solutions Manual*. New York, NY, USA: McGraw-Hill, 1993.

[11] M. Lang, "Allpass filter design and applications," *IEEE Trans. Signal Process.*, vol. 46, no. 9, pp. 2505–2514, Sep. 1998.

[12] M. F. Quélhas and A. Petraglia, "Optimum design of group delay equalizers," *Digit. Signal Process.*, vol. 21, no. 1, pp. 1–12, Jan. 2011.

[13] N. Stamenković, N. Stojanović, and G. Perinić, "Group delay equalization of polynomial recursive digital filters in maximal flat sense," *J. Circuits, Syst. Comput.*, vol. 28, no. 10, Sep. 2019, Art. no. 1950173.

[14] S. Jiang, Y. Wang, and Z. Ji, "A new design method for adaptive IIR system identification using hybrid particle swarm optimization and gravitational search algorithm," *Nonlinear Dyn.*, vol. 79, no. 4, pp. 2553–2576, Mar. 2015.

[15] W. Donald, "An algorithm for least-squares estimation of nonlinear parameters," *J. Soc. Ind. Appl. Math.*, vol. 11, no. 2, pp. 431–441, 1963.

[16] S.-T. Pan, "Evolutionary computation on programmable robust IIR filter pole-placement design," *IEEE Trans. Instrum. Meas.*, vol. 60, no. 4, pp. 1469–1479, Apr. 2011.

[17] S.-T. Pan, "CSD-coded genetic algorithm on robustly stable multiplierless IIR filter design," *Math. Problems Eng.*, vol. 2012, pp. 1–15, Mar. 2012.

[18] N. Karaboga, "Digital IIR filter design using differential evolution algorithm," *EURASIP J. Adv. Signal Process.*, vol. 2005, no. 8, pp. 1–8, Dec. 2005.

[19] R. Storn, "Designing nonstandard filters with differential evolution," *IEEE Signal Process. Mag.*, vol. 22, no. 1, pp. 103–106, Jan. 2005.

[20] N. Karaboga, A. Kalinli, and D. Karaboga, "Designing digital IIR filters using ant colony optimisation algorithm," *Eng. Appl. Artif. Intell.*, vol. 17, no. 3, pp. 301–309, Apr. 2004.

[21] N. Agrawal, A. Kumar, and V. Bajaj, "Optimized design of digital IIR filter using artificial bee colony algorithm," in *Proc. Int. Conf. Signal Process., Comput. Control (ISPCC)*, Sep. 2015, pp. 316–321.

[22] B. Majhi and G. Panda, "Development of efficient identification scheme for nonlinear dynamic systems using swarm intelligence techniques," *Expert Syst. Appl.*, vol. 37, no. 1, pp. 556–566, Jan. 2010.

[23] F. Serbet, T. Kaya, and M. T. Ozdemir, "Design of digital IIR filter using particle swarm optimization," in *Proc. 40th Int. Conv. Inf. Commun. Technol., Electron. Microelectron. (MIPRO)*, May 2017, pp. 202–204.

[24] N. Agrawal, A. Kumar, and V. Bajaj, "Design of digital IIR filter with low quantization error using hybrid optimization technique," *Soft Comput.*, vol. 22, no. 9, pp. 2953–2971, May 2018.

[25] A. Sarangi, S. K. Sarangi, S. K. Padhy, S. P. Panigrahi, and B. K. Panigrahi, "Swarm intelligence based techniques for digital filter design," *Appl. Soft Comput.*, vol. 25, pp. 530–534, Dec. 2014.

[26] Z. C. S. S. Hlaing and M. A. Khine, "Solving traveling salesman problem by using improved ant colony optimization algorithm," *Int. J. Inf. Edu. Technol.*, vol. 1, no. 5, pp. 404–409, 2011.

[27] *IEEE Standard for Digitizing Waveform Recorders*, IEEE Standard 1057-2017m (Revision of IEEE Std 1057-2007), Redline, 2018, pp. 1–313.

[28] R. Eberhart and J. Kennedy, "A new optimizer using particle swarm theory," in *Proc. MHS95. Proc. 6th Int. Symp. Micro Mach. Hum. Sci.*, 1995, pp. 39–43.

[29] W.-S. Lu, "Design of recursive digital filters with prescribed stability margin: A parameterization approach," *IEEE Trans. Circuits Syst. II, Analog Digit. Signal Process.*, vol. 45, no. 9, pp. 1289–1298, Sep. 1998.

[30] V. Plevris and M. Papadrakakis, "A hybrid particle swarm-gradient algorithm for global structural optimization," *Comput.-Aided Civil Infrastruct. Eng.*, vol. 26, no. 1, pp. 48–68, Apr. 2010.

[31] R. S. Chauhan and S. K. Arya, "An optimal design of IIR digital filter using particle swarm optimization," *Appl. Artif. Intell.*, vol. 27, no. 6, pp. 429–440, Jul. 2013.

[32] G. Dartmann, E. Zandi, and G. Ascheid, "A modified Levenberg–Marquardt method for the bidirectional relay channel," *IEEE Trans. Veh. Technol.*, vol. 63, no. 8, pp. 4096–4101, Oct. 2014.

[33] S. Yan, Q. Liu, J. Li, and L. Han, "Heterogeneous acceleration of hybrid PSO-QN algorithm for neural network training," *IEEE Access*, vol. 7, pp. 161499–161509, 2019.

YU ZHAO was born in Liaoning, China, in 1993. He received the B.S. degree in electrics and information engineering from the School of Automation Engineering, University of Electronic Science and Technology of China, Chengdu, China, in 2015, where he is currently pursuing the Ph.D. degree in electrical engineering.

His research interests include the design and theory of digital, analog, and mixed-signal processing systems, and high-speed data acquisition systems.

PENG YE was born in Sichuan, China, in 1973. He received the B.S., M.S., and Ph.D. degrees from the University of Electronic Science and Technology of China (UESTC), in 1995, 2001, and 2010, respectively.

He is currently a Professor with UESTC. His research interests include high-speed data acquisition, signal processing, and digital storage oscilloscope.

JIE MENG (Graduate Student Member, IEEE) was born in Inner Mongolia, in 1992. She received the B.S. degree from the School of Automation Engineering, University of Electronic Science and Technology of China (UESTC) Chengdu, China, in 2015, where she is currently pursuing the Ph.D. degree.

Her research orientation includes wide-band signal communication systems, digital signal processing, vector signal analysis, and high-speed signal acquisition.

KUOJUN YANG (Member, IEEE) was born in Hunan, China, in 1986. He received the B.S., M.S., and Ph.D. degrees from the University of Electronic Science and Technology of China (UESTC), in 2007, 2010, and 2015 respectively.

He is currently an Associate Professor with UESTC. His research interests include high-speed data acquisition, signal processing, and digital oscilloscope.

JIAN GAO (Member, IEEE) was born in Hebei, China, in 1993. He received the bachelor's degree from the University of Electronic Science and Technology (UESTC), Chengdu, China, in 2015, where he is currently pursuing the Ph.D. degree.

His research interests include mixed-signal processing, filter design, optimization control, high-speed ADCs, and digital storage oscilloscopes.

ZHIXIANG PAN was born in Anhui, China, in 1993. He received the B.S. degree from the School of Automation Engineering, University of Electronic Science and Technology of China (UESTC), Chengdu, China, in 2015, where he is currently pursuing the Ph.D. degree in instrument science and technology.

His research interests include the design and theory of wideband signal acquisition and processing, and electronic measurement and instrument.

WUHUANG HUANG (Member, IEEE) was born in Fujian, China, in 1983. He received the B.S., M.S., and Ph.D. degrees from the University of Electronic Science and Technology of China (UESTC), in 2007, 2010, and 2015, respectively.

He is currently an Associate Professor with UESTC. His research interests include high-speed data acquisition, signal processing, oscilloscope, and wireless sensing systems.

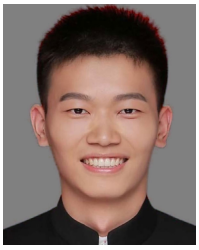

JINPENG SONG (Member, IEEE) received the B.S. and Ph.D. degrees in instrumentation and measurement science from the University of Electronic Science and Technology of China, Chengdu, China, in 2013 and 2019, respectively.

He was a Visiting Researcher with the University of Wisconsin-Madison, Madison, WI, USA, from 2016 to 2018. He is currently a Postdoctoral Research Fellow with the Beijing Institute of Technology (BIT), Beijing, China. His research interests include the design and theory of digital, analog, and mixed-signal processing systems with special emphasis on wireless communication systems and digital enhancement techniques for analog signal processing systems.

XUEFENG DAI was born in Anhui, China. He is currently pursuing the master's degree with the School of Automation Engineering, University of Electronic Science and Technology of China (UESTC).

His research interests include digital signal processing and high performance FPGA algorithm.